CHALMERS
UNIVERSITY OF TECHNOLOGY

Optical properties of water-coated sea salt model particles

Downloaded from: https://research.chalmers.se, 2021-12-11 21:31 UTC

Citation for the original published paper (version of record):
Kanngiesser, F., Kahnert, M. (2021)
Optical properties of water-coated sea salt model particles
Optics Express, 29(22): 34926-34950
http://dx.doi.org/10.1364/OE.437680

N.B. When citing this work, cite the original published paper.

research.chalmers.se offers the possibility of retrieving research publications produced at Chalmers University of Technology.
It covers all kind of research output: articles, dissertations, conference papers, reports etc. since 2004.
research.chalmers.se is administrated and maintained by Chalmers Library

(article starts on next page)

Research Article | Vol. 29, No. 22 / 25 Oct 2021 / Optics Express 34926

Optics EXPRESS

Optical properties of water-coated sea salt model particles

FRANZ KANNGIEßER[1,*] AND MICHAEL KAHNERT[1,2]

[1] Chalmers University of Technology, SE-412 96, Gothenburg, Sweden
[2] Swedish Meteorological and Hydrological Institute, Folkborgvägen 17, SE-601 76 Norrköping, Sweden
[*] franz.kanngiesser@chalmers.se

Abstract: We investigate the optical properties of marine aerosol in dependence of the water content. To this end we develop a model geometry that realistically mimics the morphological changes as the salt particles take up more water. The results are compared to morphologically simpler models, namely, homogeneous and inhomogeneous superellipsoids, as well as cube-sphere hybrids. The reference model yields depolarization ratios, depending on size and water uptake, in the range from 0 to 0.36 ± 0.12. Overall, the simple models can reproduce optical properties of the reference model. The overall nonsphericity, as well as inhomogeneity are identified as key morphological parameter, while rounding of edges only has a minor impact on optical properties.

Published by The Optical Society under the terms of the Creative Commons Attribution 4.0 License. Further distribution of this work must maintain attribution to the author(s) and the published article's title, journal citation, and DOI.

1. Introduction

Marine aerosol is emitted into the atmosphere by wind tearing off wave crests and air bubbles bursting in the oceans. Due to the vast source regions, marine aerosol is one of the most abundant aerosol types in the atmosphere [1]. Marine aerosol influences the climate directly by scattering radiation [2–4] and indirectly by acting as cloud condensation nucleii, which in turn affects cloud reflectivity and precipitation [1]. It also provides large surface areas for heterogeneous chemical reactions [2]. In coastal areas sea salt aerosol plays an important role in corrosion processes of metals and reinforced concrete structures [5]. Sea water contains a mixtures of different dissolved salts, of which sodium chloride is most abundant [6]. The composition of sea salt aerosol particles is determined by the minerals contained in the ocean's surface layer [3,7–11]. Marine aerosol may further contain biogenic material [12].

With increasing relative humidity sea salt aerosol particles grow by water condensing onto the crystal [13,14]. The condensed water increasingly dissolves the salt crystal. At a relative humidity of approximately 70 – 74% the main delinquescence point of sea salt is reached [15] and the sea salt crystal becomes fully dissolved in a liquid droplet. Partial dissolution of sea salt occurs already at lower values of RH caused by salts other than NaCl [10,16]. With decreasing relative humidity such a fully dissolved sea salt crystal remains in liquid state until the relative humidity is below approximately 45 – 50% [10,16]. At this point, the efflorescence point, the sea salt recrystallizes. As a consequence of this hysteresis effect both crystalline salt particles with a water coating and fully dissolved, hence liquid salt aerosol particles may exist between values of relative humidity of ~ 50 and ~ 70%. For comparison, pure sodium chloride's deliquescence point is at $RH = 74.0 \pm 0.2\%$ and its efflorescence point is at $43.0 \pm 1.0\%$ [17]. Thus, between values of the relative humidity between 45 and 70% both spherical droplets containing fully dissolved salt and solid, partially nonspherical salt crystals with a watery hull can exist. From laboratory measurements [18], we know that dry, crystalline salt particles ($RH = 10 - 20\%$) change the polarization state of incident laser light (linear depolarization ratios of $\delta_l = 0.21 \pm 0.02$ for sodium chloride and $\delta_l = 0.08 \pm 0.01$ for sea salt), while the polarization state is largely

#437680 https://doi.org/10.1364/OE.437680
Journal © 2021 Received 13 Jul 2021; revised 1 Oct 2021; accepted 3 Oct 2021; published 11 Oct 2021

Optics EXPRESS

unchanged by dissolved salt at RH>90% (δ_l = 0.01 ± 0.001 for both sodium chloride and sea salt). This change in linear depolarization ratio can be attributed to the transition from cube-like salt crystals to spherical droplets of fully dissolved salt.

A previous study found that the optical properties of dried sea salt aerosol particles including associated uncertainties can be modelled using convex polyhedra, a randomized class of model particles with a cube being the limiting case [19]. As a first objective, our study plans to extend this model by considering sea salt particles with a water coating. To this end, we introduce a model for water-coated salt particles that uses a pseudo-potential model in order to account for the effect that water vapor will predominantly condense onto regions on the salt crystal's surface with a large number of neighboring atoms, while salt ions in the solid phase and in contact with liquid coating will predominantly go into solution if the ions have few neighbors. The geometries constructed with this model display a gradual transition from film-coated irregular cuboid crystals to more rounded salt cores with a thick spherical liquid coating. We use this rather complex model as a reference geometry, which serves three purposes. First, we average optical properties over several realizations of the randomized geometries, which is closely analogous to what one would observe in nature. Second, by investigating the range in which the optical properties vary among different stochastic realizations of the randomized geometries, we can obtain an estimate of the model's error variance, which is an important input parameter to inverse methods, such as data assimilation (e.g. [20]). Third, by comparing this rather detailed and morphologically realistic particle to simpler geometries, we can investigate which morphological features make the dominant contributions to the optical characteristics.

In addition to convex polyhedra homogeneous sea salt aerosol particles have previously been modeled using spheres [21–25], cubes [18,23–27], elongated and flattened cuboids [24], superellipsoids [19,28], and Gaussian random cubes [19]. Spherical models usually represent dissolved sea salt, while the other shapes represent dried sea salt. A subset of these studies investigated the linear depolarization ratio [18,19,25–28]. Inhomogeneous, i.e. water-coated sea salt, was modeled with inhomogeneous cube-like and octahedra-like superellipsoids and superellipsoids embedded in a spherical shell [28]. Originally used to calculate single scattering properties, such as the linear depolarization ratios and scattering coefficients [28], these inhomogeneous models were also employed to calculate the direct radiative forcing of inhomogeneous sea salt [29] and polarized radiance at the top of the atmosphere [30].

Off-center inhomogeneities in spherical model particles can give rise to large values of the linear backscattering depolarization ratio, as studies for soot containing aerosol showed [31,32]. Here, using a non-concentric spherical shell model (see Sec. 2.2) the effect of off-center inhomogeneities on the optical properties is investigated.

Our morphologically complex and realistic reference model, which takes random deviations from a cubical shape and the changes due to water condensing onto a salt crystal into account, is computationally demanding. Operational use of lidar observations, such as processing global remote sensing data from satellites, would require a computationally less expensive model. The second aim of this study is to find a simplified model, which can simultaneously simulate optical cross sections and linear depolarization ratio.

A microphysical property hypothesized to have a key impact on the optical properties is the overall (non-)sphericity of the particles. Here both homogeneous and inhomogeneous particles are considered. In order to test this hypothesis model particles, which allow a gradual change between cubical and spherical geometries, are investigated. One particle class used, are homogeneous superellipsoids, another are inhomogeneous superellipsoids (see Sec. 2.3). Superellipsoids were previously found to be a suitable geometry type to model sea salt optical properties [19,28]. As an additional model geometry a cube-sphere hybrid model is introduced. By contrast to superellipsoids, this model results in less pronounced rounding of the cubes' edges.

To summarise, we address the following questions.

Optics EXPRESS

- If we construct a morphologically and compositionally realistic model that describes the processes of water uptake and salt dissolution based on physically plausible assumptions, how does such a model describe the change in cross sections, depolarization ratio, and lidar ratio as the salt particles take up an increasing amount of water? Within what range do the modeled optical properties vary as we alter the randomized model geometries? How do the results depend on particle size, and how do they compare to observations?
- For thickly coated, but not fully dissolved salt particles, does the positioning of the salt core inside a spherical brine coating impact the depolarization ratio? How strong is this inhomogeneity effect compared to the impact of nonspherical brine coatings on the depolarization ratio?
- Can we identify morphologically simpler model particles that are capable to mimic the change in optical properties with increasing water uptake, which we have simulated with the reference model?
- From the comparison of simpler models with the complex reference model, can we gain any insights on which morphological characteristics of marine aerosol are likely to have a major impact, and which ones will have a minor impact on the optical properties?

The particle models employed are discussed in Sec. 2. Section 3 discusses the single scattering codes used. The results are presented in Sec. 4 and discussed in Sec. 5.

2. Particle models

The basic idea is to investigate (i) how modeled optical properties of marine aerosol particles change as more and more water is taken up by the particles; and (ii) how modeled optical properties compare under different assumptions of the morphology of dry and water-coated marine aerosol particles. For each model particle the dry-particle size and the salt-volume fraction in the salt-brine composite particle are prescribed. Note that we do not make any assumptions here under which thermodynamic conditions such volume fractions would be encountered in nature. Thus the optics models are completely general and could be applied in conjunction with any parametrizations that provide the amount of water taken up by the particle as a function of temperature and relative humidity.

Four different models are used in this study: convex polyhedra with a pseudo-potential coating model, a non-concentric spherical shell model, a superellipsoidal model, and a cube-sphere hybrid model. Two different types of superellipsoids are used - homogeneous superellipsoids and inhomogeneous superellipsoids.

2.1. Reference model: Convex polyhedra with pseudo-potential coating

This class of model particles will serve as our reference geometry. The main morphological features of both the salt core and the water coating are intended to mimic those of realistic water-coated sea salt particles.

Dried sea salt particles display deviations from a perfectly cubical shape, as can be seen in images shown in [3,12,14,25,33–36]. In a previous study of dried sea salt aerosol particles convex polyhedra were found to be a suitable geometry type for modeling the optical properties of sea salt aerosols and capturing the effects of these shape deviations. Stochastic variations in the model resulted in bias-free, random errors [19] of optical properties, which can be useful for estimating model uncertainties.

Convex polyhedra are created by randomly placing a number of points N_c in a Cartesian coordinate system, and by applying a convex hull around these points [19,37]. The resulting shapes are irregular and their surfaces are composed of plane faces. N_c controls the shape. For a

Optics EXPRESS

decreasing number of N_c the shapes become increasingly non-cubical up to a point, when they introduce a bias in the optical properties. By contrast, for high values of N_c the variation in the optical properties is small, as the shapes differ only little from a cube. Intermediate values of N_c proved to be the most useful model particles. Following the results in [19] N_c is assumed to be 50, 100, and 250, respectively, and five different stochastic realizations of the geometry per value of N_c are generated. On average convex polyhedra with $N_c = 50$ fill out 58.4% of a cube's volume with an edge equally long as the respective polyhedron's largest extend along the Cartesian axes. Due to the different stochastic realizations the range of this fraction is between 54.3% and 62.1%. For $N_c = 100$ and $N_c = 250$ the polyhedra fill the corresponding cubes on average to 66.3% (full range: 64.1-69.2%) and 81.7% (full range: 79.6-84.3%), respectively. This quantifies, how the convex polyhedra become more cube-like and how the shape variation for different stochastic realisations decreases with increasing N_c.

Dry or partially coated sea salt particles in moist air can adsorb water to its surface. The water will partially or completely dissolve the salt. Microscopically, water uptake results from the Coulomb interaction of water vapor molecules with molecules or ions on the particle's surface. This interaction is likely to be stronger at those surface points that have a large number of neighboring molecules/ions. We mimic this effect by use of a simple pseudo-potential model, which has previously been used to mimic surface-tension effects in sulfate-coated soot particles [38]. This model lends itself easily to be used in conjunction with the discrete dipole approximation (see Sect. 3.1). More specifically, we assume that the volume of the particle has been discretized into N equal-size cubic volume cells of side length d. We define for each volume cell i on the particle surface a potential

$$V_i = -\sum_{j=1}^{N} f_j, \quad i = 1, \ldots, N_s \tag{1}$$

$$f_j = \begin{cases} 1 & : |\mathbf{r}_i - \mathbf{r}_j| \leq R \\ 0 & : \text{otherwise} \end{cases}, \tag{2}$$

where N_s denotes the number of volume cells on the particle surface, regardless of whether they are occupied by solid salt or by liquid water. $\mathbf{r}_i$, $\mathbf{r}_j$ are the position vectors of volume cells i and j, where the summation over j extends over the entire volume of the water-coated salt particle. The free parameter R determines the radius within which the neighboring volume cells contribute to the surface potential. The surface points are sorted by increasing surface potential, and the liquid-water volume-cells are attached starting from those surface-points with the lowest (negative) surface potential. If several surface points have equal potential, then the order in which liquid-water cells are attached is determined by a random selection.

There are several complications in this construction process. The most obvious one is that the addition of liquid water changes the surface of the particle. Thus, the surface potential needs to be re-evaluated periodically. Following the methodology in [38], this is done in a two-step process, which we abbreviate by `add_coating`:

- Step 1: Set the potential radius to $R_1 = 3d$, where d is the side-length of the cubic volume cells of the discretized particle. Compute the surface potential, and attach $N_{\text{add}} = \alpha_1 N_s$ liquid water cells to the surface, starting with the surface points of lowest potential (corresponding to the strongest Coulomb interaction). We set $\alpha_1 = 0.004$.

- Step 2: Recompute the surface potential with $R = \max\{R_1, R_{\text{cor}}\}$, where $R_{\text{cor}} = (d^2/R_{\text{V}})\sqrt{3N/(2\pi) - 1}$, and R_{V} is the volume-equivalent radius of the particle. (Note that N and N_s have changed after step 1.) Then apply an additional $N_{\text{add}} = \alpha_2 N_s$ liquid-water

Optics EXPRESS

cells to the surface, starting again from the surface points with the lowest potential. We use $\alpha_2 = 0.001$.

In this approach we largely follow the suggestions in [38]. However, with the settings given in [38] for α_1 and α_2, our large water-coated salt particles do not become spherical. Our settings of $\alpha_1 = 0.004$ and $\alpha_2 = 0.001$ ensure that the water-coating makes a smooth transition from a nonspherical thin film to a thick spherical coating as more and more water is applied to the surface.

The two-step process that we labeled `add_coating` would need to be repeated until the total amount of liquid coating material has been applied. However, there is a second complication that we need to consider first. The salt core is water soluble, by contrast to the insoluble soot particles considered in [38]. We assume that the salt solution is saturated, where the solubility of sodium chloride at 283 K has been used, which is 36 g NaCl per 100 ml water. We further assumed that sea salt has a density equal to that of NaCl, 2240 kg/m^3, and that the brine coating has a density of 1210 kg/m^3. This determines, at each step of the coating process, the number of volume cells that are removed from the salt core, and the number of volume cells that are to be added to the coating due to the addition of the solute. Microphysically, those salt ions on the solid surface in contact with water that experience the weakest Coulomb interaction with their surrounding are most likely to go into solution. We model this by use of the surface-potential model given in Eqs. (1) and (2), where N_s now denotes the number of salt cells that lie on the water-covered part of the solid-particle surface, and where the sum over j extends over all grid cells that contain solid salt. We define an algorithm analogous to the one discussed above, but based on the points of *highest* potential (corresponding to the weakest Coulomb interaction). We denote this process by `dissolve_salt`:

- Step 1: Set $R_1 = 3d$ and dissolve $N_{\text{dis}} = \beta_1 N_s$ salt cells (where N_s now denotes the number of only those solid surface points that are in direct contact with the liquid coating). The dissolution of liquid-covered surface cells proceeds in the order of *decreasing* surface potential.
- Step 2: Recompute the surface potential with $R = \max\{R_1, R_{\text{cor}}\}$. Then dissolve $N_{\text{dis}} = \beta_2 N_s$ surface cells, starting from those with the *highest* potential.

Here we set $\beta_1 = 0.0016$ and $\beta_2 = 0.0004$.

The complete algorithm starts from a prescribed dry particle size and a target salt-volume fraction for the brine-coated particle. This predetermines the number N_w of water-cells that are to be added (as well as the number of salt-cells that need to be dissolved). Then the iteration proceeds by the following scheme.

```
DO WHILE Nw(now)<Nw
    add_coating
    dissolve_salt
END DO
```

N_w(now) denotes the number of water-cells that are presently applied at any given step of the iteration. The important point is that the surface potential, which determines the attachment of water and the dissolution of salt, is frequently updated in this iteration. This is controlled by α_1, α_2, β_1, β_2.

The model geometries are illustrated in Fig. 1 for a polyhedron with $N_c = 100$. The values of f_{vol} decrease from left to right with $f_{\text{vol}} = 1.0$ (left), $f_{\text{vol}} = 0.8$, $f_{\text{vol}} = 0.55$, and $f_{\text{vol}} = 0.3$ (right). The original dry particle (left) is generally irregular but similar to a cube, depending on the choice of N_c. Adsorption of a small amount of water results in a thin film coating that closely follows the shape of the salt core (second from left). We see already at this early stage of the coating process that the sharp edges of the salt particle become slightly rounded off, because

Optics EXPRESS

the solid volume cells along the edges, which have few neighbors, have a high surface potential and go quickly into solution. As more water is applied the rounding of the edges becomes more pronounced and the coating approaches spherical shape (second from right). For thickly coated particles both the coating and the salt core become spherical (right). Application of even more water will result in spherical particles in which the salt has become completely dissolved (not shown). This model has a number of free parameters. The settings we chose for our reference model are meant to qualitatively mimic the behavior in real atmospheric sea-salt particles. In particular, if α_1, α_2 are too large, then the coating does not reach spherical shape.

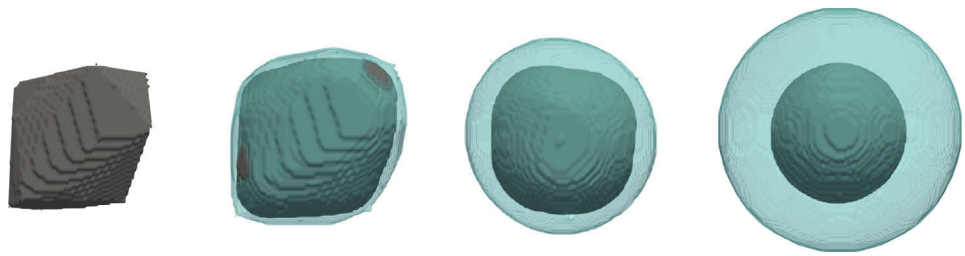

Fig. 1. Example for a coated convex polyhedron (N_c = 100) with different values of f_{vol}, from left to right - f_{vol} = 1.0, f_{vol} = 0.8, f_{vol} = 0.55, and f_{vol} = 0.3.

2.2. Non-concentric spherical shell model

Calculations of the energy potential of solid inclusions in liquid droplets suggest, that such inclusions are predominantly moved towards the droplet's surface [39]. Thus, the inclusions have an off-center position. The impact of the resulting off-center inhomogeneities on the optical properties is investigated using a non-concentric spherical core-shell model, based on [40]. The non-concentric spherical shell models aim at investigating a potential refinement of the coated polyhedra model. The inner sphere represents the salt core, which is encapsulated by a shell representing saturated salt solution. The radii of both spheres correspond to the volume equivalent radii of the entire particle and its solid core as determined with the coated convex polyhedra model. The inner sphere's center is shifted with respect to the shell's center, but constrained to always lie within the spherical shell. The relative shift of the core's center s_{rel} is expressed as fraction of the shell's radius. As f_{vol} decreases, the possible range of s_{rel} increases.

A similar model was used in [31] for modelling the linear depolarization ratios of coated soot. The non-concentric spherical core shell model used in this study differs in the variable size of the core, reflecting the slowly dissolving salt crystal, from the version used in [31].

A schematic of the model is shown in Fig. 2. With decreasing f_{vol} (as indicated by the rows, from top to bottom), increasing relative shifts are possible (indicated by the columns, increasing from left to right.)

For the non-concentric spherical shell model values of f_{vol} ranging from 1.0 to 0.15, with a linear spacing of Δf_{vol} = 0.05 are considered. In addition f_{vol} = 0.139 is also considered. For smaller values, the salt core becomes fully dissolved. The shift of the core s_{rel} is, starting from s_{rel} = 0.0, increased by Δs_{rel} = 0.025. This results in 228 different combinations of f_{vol} and s_{rel}, for which the core is placed within the hull.

2.3. Superellipsoids

Superellipsoids have previously been used to model mineral dust [41,42] and sea salt aerosol [19,28,29]. Superellipsoids describe three-dimensional shapes as the product of two superquadratic curves [43,44]. They can be considered a generalization of ellipsoids and are

Optics EXPRESS

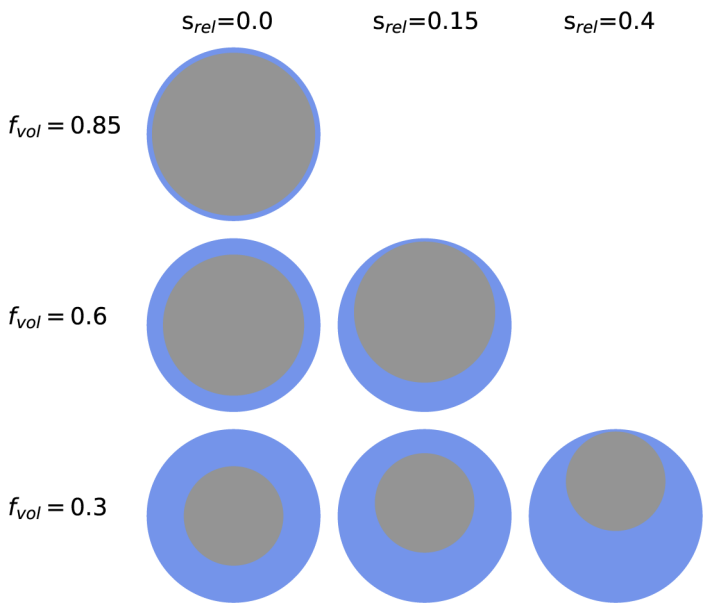

Fig. 2. Schematic of the non-concentric spherical shell model. The salt core is shown in grey and the watery shell in blue. The different rows represent different salt fractions f_{vol} and the columns different relative displacements of the salt core with respect to the watery shell.

represented in the Cartesian coordinate system by [44]

$$\left[\left(\frac{x}{a}\right)^{\frac{2}{e}} + \left(\frac{y}{b}\right)^{\frac{2}{e}}\right]^{\frac{e}{n}} + \left(\frac{z}{c}\right)^{\frac{2}{n}} = 1 \tag{3}$$

Here a, b, and c determine the particle's extent along the Cartesian axes x, y, and z, respectively. The particle's shape is specified by n and e, the roundness parameters in the north-south (or polar) and east-west (or azimuthal) directions, respectively [41,44]. This makes superellipsoids a highly versatile type of geometry, allowing to obtain cubes, spheres, cylinders and octahedra by just changing the roundness parameters. An explicit parameterization of superellipsoids in spherical coordinates has recently been derived and applied in [19].

In the present study $a = b = c$ is assumed, i.e. the respective aspect ratios are $a/c = b/c = 1$. Nevertheless, the term superellipsoids will be used throughout this study. Following the approach by [41] $n = e$ is assumed. The range of $n = e$ is further limited to 0 (cubes) – 1 (spheres). During the process of water adsorption and the ensuing dissolution of the sea salt crystal the shape changes from nearly cubical to spherical (with inclusions) and eventually to a homogeneous sphere. This highlights the potential suitability of superellipsoids to approximate the reference model for different values of f_{vol} and hence the different resulting overall shapes. Here, two different types of superellipsoids were used - homogeneous and inhomogeneous superellipsoids. Investigating both homogeneous and inhomogeneous superellipsoids allows us to study simultaneously non-sphericity and inhomogeneity and the respective impact on the optical properties. For homogeneous superellipsoids an effective refractive index for a mixture of sodium chloride and a staturated sodium chloride solution is determined using the Maxwell-Garnet mixing rule [45]. Inhomogeneous superellipsoids consist of an outer layer representing a saturated sodium chloride solution and a sodium chloride core. Both the outer layer and the core possess the same roundness parameters. The layer's thickness is determined by the salt volume fraction.

Optics EXPRESS

Figure 3 shows examples for the two types of superellipsoids employed in this study. The roundness parameter increases from left to right, so that the shapes become increasingly spherical. The top row shows homogeneous superellipsoids, i.e., they have a core fraction of $f_{\mathrm{vol}} = 1.0$. The bottom row shows inhomogeneous superellipsoids with a core fraction of $f_{\mathrm{vol}} = 0.55$. The solid fraction is represented by dark grey and the liquid fraction by light-blue. For both inhomogeneous and homogeneous superellipsoids the calculations are performed for eleven different values of n ranging from $n = 0.0$ to $n = 1.0$ with $\Delta n = 0.1$, and for nine different values of f_{vol}, ranging from $f_{\mathrm{vol}} = 1.0$ to $f_{\mathrm{vol}} = 0.3$, with $\Delta f_{\mathrm{vol}} = 0.1$ as well as for $f_{\mathrm{vol}} = 0.55$.

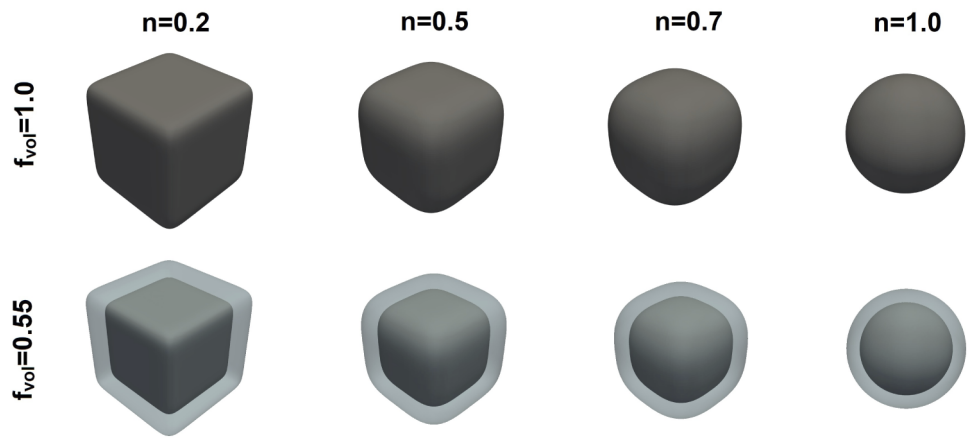

Fig. 3. Examples for superellipsoids with two different solid fractions $f_{vol} = 1.0$ (top row) and $f_{vol} = 0.55$ (bottom row) as used in this study. The roundness parameter n of the superellipsoids increases from left to right.

2.4. Cube-sphere hybrids

The superellipsoids are an extremely versatile class of model particles. However, while easy to implement in the discrete dipole approximation, using them in Waterman's T-matrix method [46] poses some challenges. In that method one employs the surface parameterization $r_{\mathrm{s}}(\theta, \phi)$ of the particle surface, as well as its partial derivatives $\partial r_{\mathrm{s}}/\partial\theta$ and $\partial r_{\mathrm{s}}/\partial\phi$. Here, (θ, ϕ) denote spherical coordinates. This is important, as Waterman's method is based on the use of vector spherical wave functions defined in spherical coordinates. Neither the implicit parameterization given in Eq. (3), nor explicit parameterizations in other coordinate systems, such as the one found in [44], can be readily used in Waterman's method. To the best of our knowledge, the first derivation of $r_{\mathrm{s}}(\theta, \phi)$, $\partial r_{\mathrm{s}}/\partial\theta$, and $\partial r_{\mathrm{s}}/\partial\phi$ for superellipsoids, as well as its application in the T-matrix method, has been reported only very recently [19].

A much simpler alternative are cube-sphere hybrids. Let us denote the surface parameterization of a cube by $r_{\mathrm{c}}(\theta, \phi)$, and let r_0 denote the radius of a volume-equivalent sphere. We define the surface parameterization of the cube-sphere hybrid by

$$r_{\mathrm{csh}}(\theta, \phi) = [(1-\eta) r_{\mathrm{c}}^3(\theta, \phi) + \eta r_0^3]^{1/3} \tag{4}$$

$$\frac{\partial r_{\mathrm{csh}}(\theta, \phi)}{\partial\theta} = (1-\eta)\frac{r_{\mathrm{c}}^2}{r_{\mathrm{csh}}^2}\frac{\partial r_{\mathrm{c}}}{\partial\theta} \tag{5}$$

$$\frac{\partial r_{\mathrm{csh}}(\theta, \phi)}{\partial\phi} = (1-\eta)\frac{r_{\mathrm{c}}^2}{r_{\mathrm{csh}}^2}\frac{\partial r_{\mathrm{c}}}{\partial\phi}. \tag{6}$$

Optics EXPRESS

where $0 \leq \eta \leq 1$. For $\eta = 0$ we obtain a cube, for $\eta = 1$ we obtain a sphere, and for intermediate values we obtain hybrid particles as indicated in Fig. 4. The volume-equivalent radius of these hybrid particles is equal to r_0, regardless of the choice of η.

Fig. 4. Cube-sphere hybrid particles, in which the parameter η is, from left to right, 0.1, 0.3, 0.5, 0.7, and 0.9. The cube ($\eta = 0.0$) and the sphere ($\eta = 1.0$) are not shown.

As a side-note, we could equally well have defined the hybrid by a linear superposition of the radii, i.e., $r_{\mathrm{csh}}(\theta, \phi) = (1 - \eta)r_{\mathrm{c}}(\theta, \phi) + \eta r_0$. As long as both the cube and the sphere have the same volume, the hybrid particle will also have the same volume. However, if $r_{\mathrm{c}}^3 \neq r_0^3$, i.e., when the cube and the sphere have different volumes, then the volume of the composite particle and its volume-equivalent radius will be easiest to compute from Eq. (4).

3. Computational methods

To obtain the single scattering properties three different codes are used - the discrete dipole approximation code ADDA and the T-matrix codes MSTM and Tsym.

The single scattering codes return the scattering matrix F and the optical cross sections. From these quantities the linear depolarization ratio in the backscattering direction can be calculated by [47]:

$$\delta_l = \left.\frac{F_{11} - F_{22}}{F_{11} - F_{22}}\right|_{\theta=180^\circ} \tag{7}$$

F_{11} and F_{22} denote the (11) and (22) element of the scattering matrix, respectively. The matrix elements are evaluated in the backscattering direction ($\theta = 180^\circ$).

The extinction-to-backscatter ratio, in context of lidar remote sensing also referred to as lidar ratio, can be calculated by [48]

$$S_p = 4\pi \left.\frac{C_{ext}}{C_{sca}F_{11}}\right|_{\theta=180^\circ}. \tag{8}$$

Here C_{ext} denotes the extinction cross section. The backscattering cross section is expressed by $\frac{1}{4\pi}C_{sca}F_{11}\big|_{\theta=180^\circ}$.

The calculations were performed for a wavelength of $\lambda = 0.532\,\mu$m, the second harmonic of Nd:YAG lasers. Nd:YAG lasers are commonly used in lidar remote sensing [49,50]. The refractive index of salt was assumed to be equal to the refractive index of sodium chloride, $m_{NaCl} = 1.5484 + i0$ [51]. In accordance with the reference model, the liquid hull was assumed to consist of a saturated solution of NaCl in water (brine), for which we used a refractive index $m_{NaCl,sol} = 1.3174 + i6.19 \cdot 10^{-7}$ [52].

3.1. ADDA

The discret dipole approximation (DDA) code ADDA, version 1.3b4 [53,54], was used to calculate optical properties of the coated polyhedra and the inhomogeneous superellipsoids.

The DDA divides the scatterer into a number of small, fully polarisable volume-elements much smaller than the wavelength. These volume-elements are referred to as dipoles. Owing to this dividing the scatterers into dipoles the DDA can treat arbitrarily shaped and inhomogeneous

Optics EXPRESS

particles. The dipole spacing d was chosen, following uncertainty estimates discussed in [19], so that $|m|kd = 0.38$. Here m denotes the complex refractive index and k the wavenumber of incident light. This corresponds to a values of dipoles per wavelength of $dpl = 25.5$.

Orientation averaging is required as the scatterers are assumed to be totally randomly orientated. Orientation averaging is performed in ADDA over the three Euler angles α, β, and γ using Romberg integration. The set of integration points is defined by the minimum and maximum value and the number of subdivisions $J_{\min}$ and $J_{\max}$. For the coated convex polyhedra $J_{\max}$ for α and γ was chosen to be $J_{\max} = 4$ and for β to be $J_{\max} = 3$. With the number of arguments of the integration limited to $2^{J_{\min}} + 1$, this results in 2601 discrete orientations. In case of the inhomogeneous superellipsoids a higher angular resolution was used, with $J_{\max} = 6$ for α and $J_{\max} = 5$ for β and γ. This choice was motivated by the sensitivity study in [19] to obtain a better agreement of the linear depolarization ratios of homogeneous superellipsoids, which was calculated using the T-matrix code Tsym , and inhomogeneous superellipsoids in the shared limiting case of $f_{\text{vol}} = 1.0$.

The scattering matrix elements were calculated with an angular resolution of 0.5°. As an iterative solver the quasi minimal residual solver QMR2 was used. Other than that ADDA default settings were used.

3.2. MSTM

The multiple sphere T-matrix code MSTM, version 3.0 [55], was employed to compute optical properties of non-concentric spherical shell particles. This code is based on the superposition T-matrix method. The method and consequently the MSTM code itself can be applied to scatterers consisting of multiple spheres with non-overlapping surfaces. This implies, that the surfaces of any two spheres may at most share a single point. The code iteratively solves the interaction equation and computes the orientation-averaged optical properties from the T-matrix by using analytical solution to the integration over Euler angles.

3.3. Tsym

Optical properties of homogeneous superellipsoids and of cube-sphere hybrid particles where computed by use of the T-matrix code Tsym, version 6.6. This code is based on Waterman's null-field method (also known as the extended boundary condition method). The code exploits symmetries of the particle geometry by (i) using the commutation relations of the T-matrix to reduce CPU-time requirements [56,57], and (ii) making use of irreducible representations of the symmetry group [58] in order to reduce numerical ill-conditioning problems, but also to further cut down the computation time. Orientation-averaged optical properties are computed by use of analytic expressions as described in [59,60]. The latest release version 5.2 of the code is described in [61] and published in [62]. The cube-sphere hybrid particles have been added in version 5.7, but results obtained with that model are published here for the first time. Superellipsoids have been added in version 6.6. This required us to derive the surface parameterization of superellipsoids in spherical coordinates, as well as its partial derivatives. The derivation as well as a first test of Tsym in conjunction with superellipsoids have been published in [19].

4. Results

4.1. Coated polyhedra

The results obtained with the reference model are shown in Fig. 5. The columns refer to the different optical properties, from left to right: δ_l, C_{bak}, C_{ext}, and S_p. The rows refer to the different radii of the dry salt particle r_0, with $r_0 = 0.33\,\mu$m, $r_0 = 0.67\,\mu$m, and $r_0 = 1.0\,\mu$m from top to bottom. The colors indicate the arithmetic means over the different values of N_c with $N_c = 50$ (orange), $N_c = 100$ (green), and $N_c = 250$ (magenta). The corresponding error bars

Optics EXPRESS

indicate the maximum range of results obtained for five stochastic realizations of the geometry for each instance of N_c. The arithmetic mean over all values of N_c and all stochastic realizations is shown in blue. Note, that the corresponding blue error bar denotes the standard deviation over all realizations and all values of N_c.

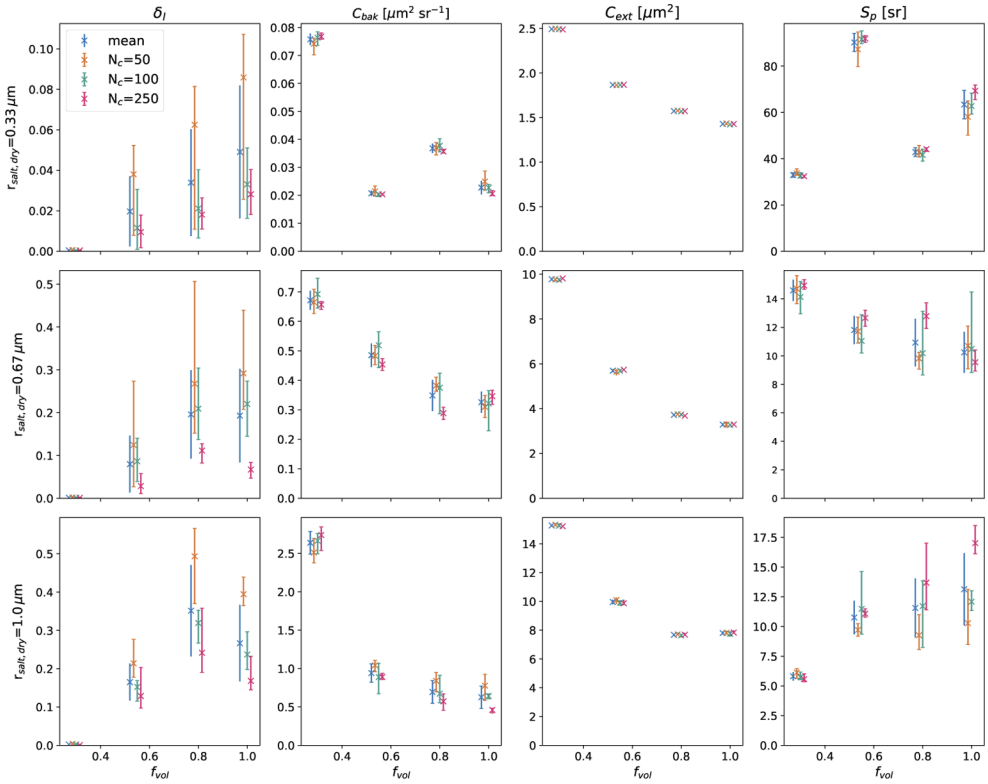

Fig. 5. Results of the reference model, i.e. depolarization ratio δ_l, backscattering cross section C_{bak}, extinction cross section C_{ext}, and extinction-to-backscatter ratio S_p (columns from left to right) for $r_0 = 0.33\,\mu$m (top row), $r_0 = 0.67\,\mu$m (middle row), and $r_0 = 1.0\,\mu$m (bottom row) at $\lambda = 0.532\,\mu$m. The results for $N_c = 50$ are shown in orange, for $N_c = 100$ in green, $N_c = 250$ in magenta. Blue denotes the mean over all three values of N_c. Error bars denote the total range and in case of the mean over N_c (blue) the standard deviation.

For each value of r_0 and f_{vol} the mean linear depolarization ratio decreases with increasing N_c. For $r_0 = 0.33\,\mu$m and $r_0 = 0.67\,\mu$m the range of δ_l also decreases with increasing N_c. Both effects can be attributed to the fact that model particles become, on average, more cube-like with increasing N_c, as reported in [19]. Regular cubes depolarize less than distorted, irregular cubes. Further, for increasing values of N_c the stochastic deviations from cubic shape become less pronounced than for low values of N_c, resulting in a reduced variability in depolarization ratios.

For larger particles, especially for $r_0 = 1.0\,\mu$m, we observe an initial increase in the linear depolarization ratio as f_{vol} is reduced from 1.0 to 0.8. This is most likely caused by an increase in particle size without a significant change in the overall shape. This observation is consistent with results reported in [28], according to which a water coating without shape changes increases the linear depolarization ratio for single particles with size parameters of up to $x = 15$, which corresponds to $r_{\text{eq}} = 1.27\,\mu$m for a wavelength of $\lambda = 0.532\,\mu$m. With further condensation

Optics EXPRESS

on the particle the linear depolarization ratio decreases as the particles become increasingly rotationally symmetric (see Fig. 1 for an example of changing particle morphology).

For $r_0 = 0.33\ \mu$m a minimum in C_{bak} and correspondingly a maximum in S_p can be observed for $f_{\text{vol}} = 0.55$. To investigate this feature the optical calculations were repeated for an increased resolution of f_{vol} with $\Delta f_{\text{vol}} = 0.05$. The results of these calculations are shown in Fig. 6. The panels show the different optical properties, the linear depolarization ratio (top left), the backscattering cross section (top right), the extinction cross section (bottom left), and the extinction-to-backscatter ratio (bottom right). The colors are as in Fig. 5. The shading represents the total range of values and in case of the properties averaged over all N_c they represent the standard deviation. For an easier interpretation only the standard deviation over all N_c is shown for C_{bak} and S_p. The morphology induced differences in C_{ext} are too small to be distinguishable. The higher resolution of f_{vol} reveals the minimum of C_{bak} and consequently the maximum of S_p to be at $f_{\text{vol}} = 0.45$. The gradual change in C_{bak} and S_p indicates that the behavior can likely be attributed to resonances in the backscattering cross section.

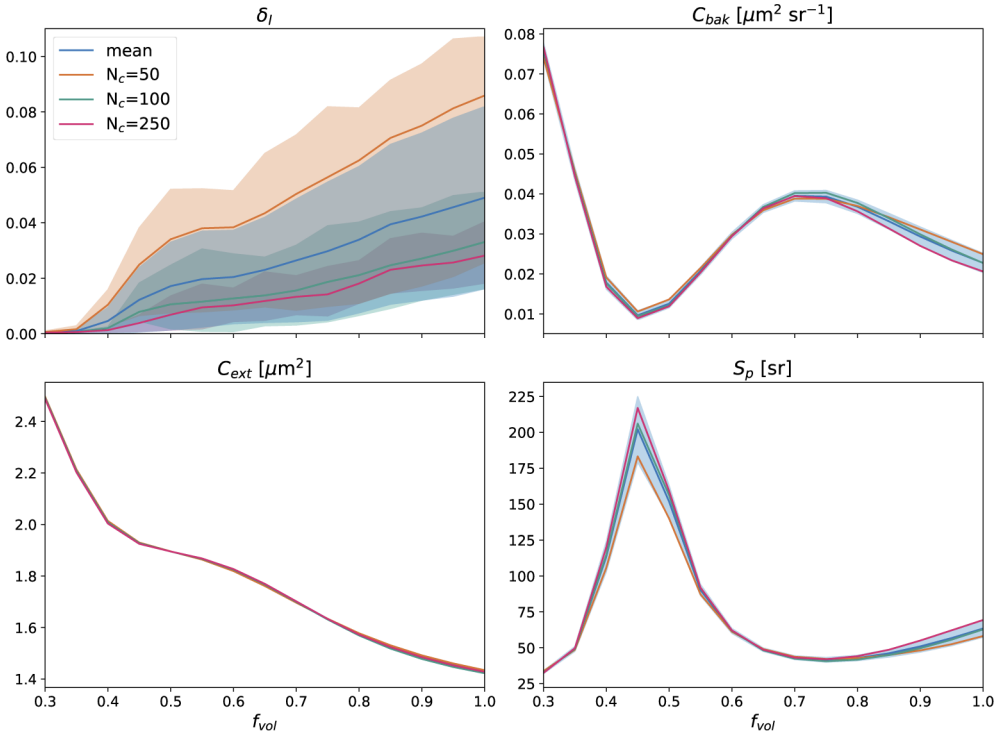

Fig. 6. Results of the coated convex polyhedra model for $r_0 = .33\ \mu$m and $\Delta f_{\text{vol}} = 0.05$. The panels show the linear depolarization ratio (top left), the backscattering cross section (top right), the extinction cross section (bottom left), and the extinction-to-backscatter ratio (bottom right). The colors are as in Fig. 5. The shading represents the the total range and in case of the mean over N_c the standard deviation. For C_{bak} and S_p only the standard deviation is shown. For C_{ext} the respective ranges are too small to distinguish by eye.

Finally, the particle grows with increasing coating thickness, i.e. decreasing f_{vol}. The resulting increase in geometric cross section entails an increase of the optical cross sections C_{bak} and C_{ext}. Thus we see that this morphologically realistic particle model yields optical properties that closely correspond to how one would expect dry and coated marine aerosol to vary with size and volume fraction.

Optics EXPRESS

4.2. Non-concentric spherical core shell

The results for the non-concentric spherical core shell model are displayed in Fig. 7. Here the rows represent the different values of r_0, with $r_0 = 0.33\,\mu$m in the top row, $r_0 = 0.67\,\mu$m in the center row, and $r_0 = 1.0\,\mu$m in the bottom row. The columns represent the different optical quantities, which are from left to right δ_l, C_{bak}, C_{ext}, and S_p. The y-axis in each panel denotes the relative shift of the core's center with respect to the shell's center, with no shift at the top and maximum shift at the bottom. The x-axis represents the salt volume fraction f_{vol}, which increases from left to right. Blank areas in the individual panels indicate the range of values for relative shifts inaccessible due to the constraint of having non-overlapping spheres.

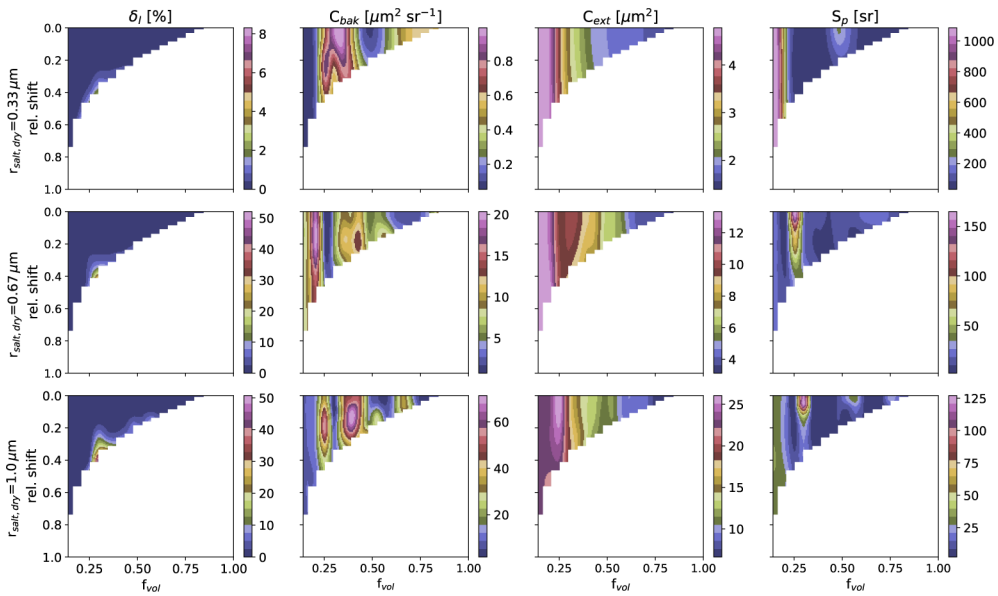

Fig. 7. Optical properties at a wavelength of $\lambda = 0.532\,\mu$m obtained by the non-concentrical spherical shell model. The columns correspond to the optical properties, these are from left to right: linear depolarization ratio, backsattering cross section, extinction cross section and extinction-to-backscatter ratio. The rows refer to the different initial sizes of the dry, uncoated particle, with $r_0 = 0.33\,\mu$m, $r_0 = 0.67\,\mu$m, and $r_0 = 1.0\,\mu$m in the top, center, and bottom row, respectively. The optical properties are shown as functions of the salt volume fraction f_{vol} and the relative shift.

Along the y-axis the linear depolarization ratio behaves as expected. The larger the relative shift of the two spheres, the stronger the deviation from spherical symmetry, resulting in higher depolarization ratios. Along the x-axis two counteracting effects can be observed. The smaller f_{vol}, the higher the water uptake. This gives the salt core more freedom to shift away from the center position, resulting in higher depolarization ratios. On the other hand, more water uptake also results in a shrinking of the salt core, as more solid material goes into solution. If the size of the inner sphere decreases beyond a certain point the solid core becomes too small to induce larger values of the depolarization ratio. For values of $f_{\text{vol}} \approx 0.3$ the depolarization ratio reaches its maximum of $\sim 50\%$. This peak value is achieved at the maximum possible relative shift. For larger coating thickness, i.e. smaller values of f_{vol} the decrease in core size results in reduced depolarization.

The backscattering cross section displays characteristic oscillations with varying f_{vol}, which is similar to the behavior we already noted in Fig. 9 for the reference geometry. For $r_{\text{salt,dry}}$=1 μm (bottom row), we can also discern corresponding oscillations along the y-axis. It is not surprising

Optics EXPRESS

that a differential scattering property, such as C_{bak}, exhibits such a high sensitivity to small changes in morphological properties.

The extinction cross section appears to be mainly controlled by the increase in particle size with decreasing f_{vol}. For the extinction-to-backscatter ratio at $r_0 = 0.67\,\mu$m and $r_0 = 1.0\,\mu$m the highest values are found at $f_{vol} \approx 0.3$. In case of $r_0 = 0.67\,\mu$m this maximum appears to be caused by the minimum of the backscattering cross sections. For $r_0 = 1.0\,\mu$m a local minimum of C_{bak} coincides with the maximum of C_{ext}.

Figure 8 shows depolarization ratio (top left panel), extinction-to-backscatter ratio (top right), extinction cross section (bottom left), and backscattering cross section (bottom right) obtained from the non-concentric spherical core shell model with $r_0 = 1.0\,\mu$m, and $f_{\text{vol}} = 0.45$ (blue line), $f_{\text{vol}} = 0.30$ (orange line), and $f_{\text{vol}} = 0.15$ (green line). As we already saw in Fig. 7 δ_l is largest for the highest relative shifts, i.e. for cores placed as closely as possible to the shell's surface. C_{ext} is mainly controlled by the particle size, which grows with decreasing f_{vol}. The increase and the decline in C_{bak} for vol = 0.15 and for $f_{\text{vol}} = 0.3$, respectively, for inclusions comparatively close to the shell's surface, can be attributed to changes of the F_{11}-element in the backscattering direction, caused by resonances. By contrast, C_{ext}, which is equal to C_{sca} (since the material is non-absorbing), displays only small changes for the range of relative shifts.

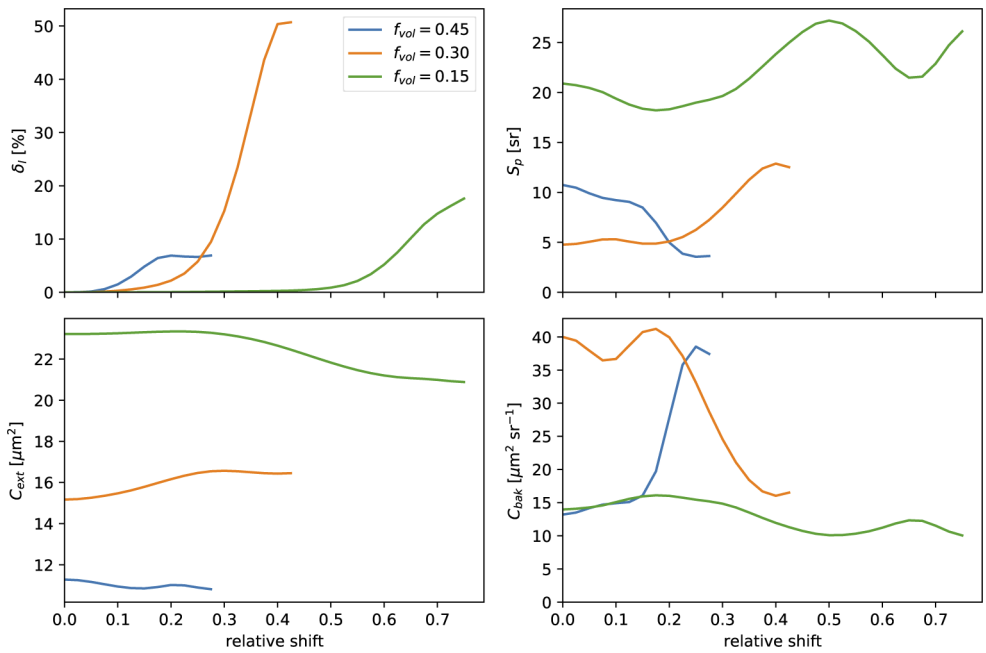

Fig. 8. Optical properties from the non-concentrical spherical shell model for $r_0 = 1.0\,\mu$m, and $f_{\text{vol}} = 0.45$ (blue line), $f_{\text{vol}} = 0.30$ (orange line), and $f_{\text{vol}} = 0.15$ (green line). The panels show the different optical properties - depolarization ratio (top left), extinction-to-backscatter ratio (top right), extinction cross section (bottom left), and backscattering cross section (bottom right).

4.3. Superellipsoids and cube-sphere hybrids

Figures 9–11 show the results for the homogeneous superellipsoids (left column), the inhomogeneous superellipsoids (center column), and the cube-sphere hybrids (right column). In each individual panel f_{vol} increases from left to right, i.e., the water amount decreases from left to right, where the rightmost values correspond to dry particles. The shape changes are represented by the

Optics EXPRESS

y-axis, with the bottom (with $n = 0 = \eta$) corresponding to a cube and the top (with $n = 1 = \eta$) corresponding to a sphere.

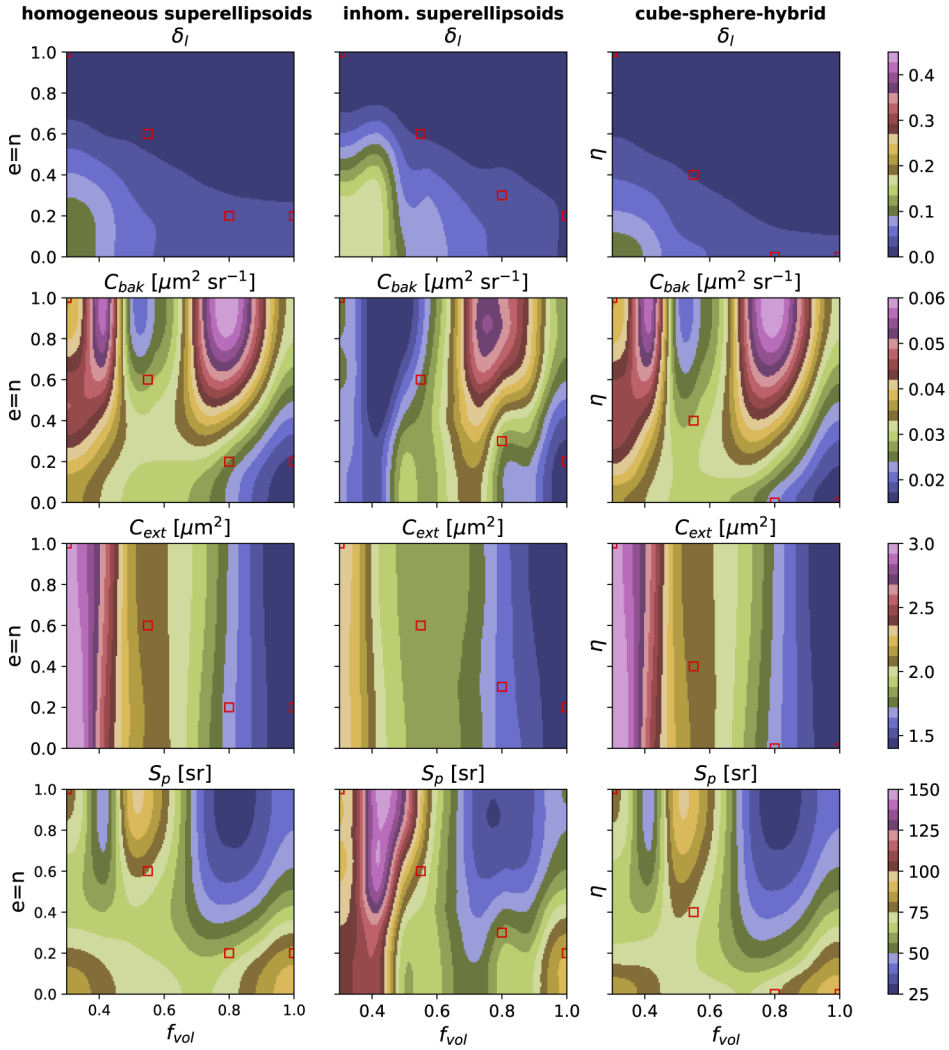

Fig. 9. Optical properties calculated with homogeneous superellipsoids (left column), coated superellipsoids (center column), and cube-sphere hybrids (right column) for $r_0 = 0.33\ \mu$m at a wavelength of $\lambda = 0.532\ \mu$m. The rows show the different optical properties, as in Fig. 7. The red squares indicate the value and the position on the y-axis for the best fit.

With increasing amount of water, i.e. decreasing f_{vol}, C_{ext} increases. This can be attributed to the increase in size due to the added water. For r_0=0.33 and 0.67 μm, no significant dependence of C_{ext} on the rounding parameters n or η can be observed. For r_0=1.0 μm, only a very weak decrease in C_{ext} with increasing roundness can be seen.

For $r_0 = 0.33\ \mu$m, δ_l increases with decreasing n and η, i.e. decreasing sphericity, and with decreasing f_{vol}. For larger values of r_0, the dependence of δ_l on f_{vol} and n displays an increasingly complex pattern of resonance features. But for all sizes, volume fractions, and model particles, δ_l converges to zero as the particles approach spherical shape ($n = \eta = 1$). Note, that the values of $\delta_l \geq 0.45$ for the inhomogeneous superellipsoids at $r_0 = 0.67\ \mu$m and $r_0 = 1.0\ \mu$m extend to $\delta_l = 0.6$.

Optics EXPRESS

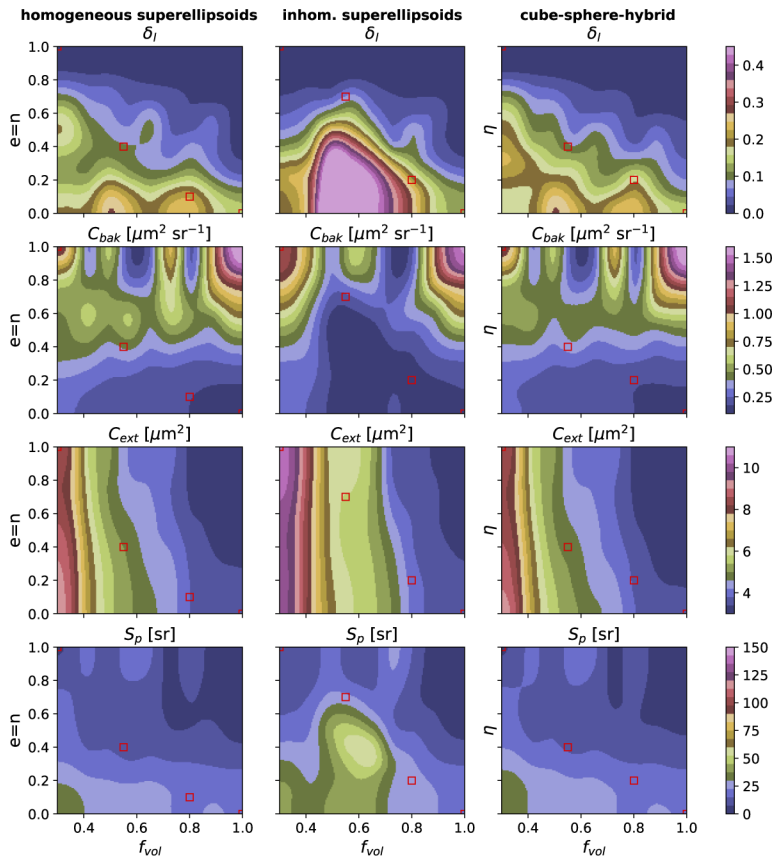

Fig. 10. As Fig. 9, but for $r_0 = 0.67\ \mu$m.

The backscattering cross section displays distinct size-dependent (i.e., f_{vol}-dependent) resonances that increase in amplitude as the particles approach spherical shape ($n, \eta \to 1$). For nonspherical, cube-like particles ($n, \eta \to 0$) such resonances are quenched by taking an ensemble average over random orientations. This effect is particularly evident for r_0=0.67 μm (Fig. 10). These resonances also affect the extinction-to-backscatter ratio, which is composed of the extinction and the backscattering cross sections. Local minima of C_{bak} generally coincide with local maxima of S_p and vice versa.

A comparison of the three columns in Figs. 9–11 allows us to identify similarities and differences among the three classes of model particles. First, we see that differences become more pronounced with increasing r_0, which was expected. Second, we find that homogeneous superellipsoids and cube-sphere hybrids display a lot more similarities in optical properties than one may have expected. This indicates that the change in overall shape has a much more profound impact on the optical properties, especially on depolarization, than the local rounding of the particles' edges. The change in overall shape is similar in both models, while the edge-rounding effect is present in superellipsoids and absent in the cube-sphere hybrids. Third, we observe that differences between homogeneous and inhomogeneous superellipsoids (columns 1 and 2) are more distinct than corresponding differences between homogeneous superellipsoids and cube-sphere hybrids (columns 1 and 3). This observation is valid for δ_l, C_{bak}, and it is particularly pronounced for S_p. This somewhat unexpected result shows that, despite the relatively low optical

Optics EXPRESS

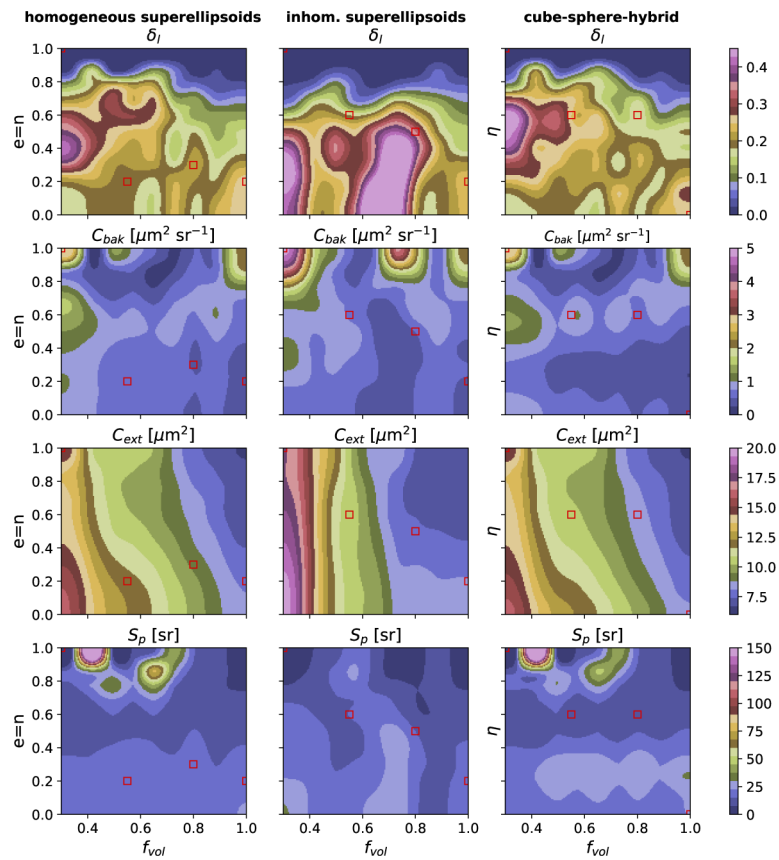

Fig. 11. As Fig. 9, but for $r_0 = 1.0\,\mu$m.

contrast between the salt core and the brine coating, inhomogeneity can have a distinct effect on lidar-relevant optical properties.

The inhomogeneous superellipsoids can yield higher values of δ_l, compared to homogeneous superellipsoids. This confirms the results reported by [28].

For each value of f_{vol} and r_0 the values of n and η best replicating the mean values of δ_l, C_{bak} and C_{ext}, as obtained from the coated convex polyhedra model, are identified. For this the geometric mean error is introduced:

$$\Delta = \sqrt{\frac{1}{3}\sum_{k=1}^{3}\left(\frac{Q_k^{\mathrm{ref}} - Q_k^{\mathrm{model}}}{Q_k^{\mathrm{ref}}}\right)^2} \tag{9}$$

For each optical property Q_k the relative differences between the coated polyhedra model as reference model and the respective simplified model, as indicated by the superscripts, are calculated. The sum extends over the three optical properties Q_k=δ_l, C_{bak}, and C_{ext}. (The lidar ratio is not included in the summation, because it is merely a quantity derived from C_{bak} and C_{ext}.) The best fit is obtained by choosing for each value of f_{vol} and r_0 the superellipsoid's roundness parameter n or in case of the cube-sphere hybrids the value of η, for which Δ has a minimum.

In Figs. 9–11 the roundness parameter n or in case of the cube-sphere hybrid η minimising Δ is indicated by a red square. Generally, with decreasing f_{vol} the superellipsoids and cube-sphere hybrids giving the best fit become increasingly spherical. This reflects the increasingly spherical

Optics EXPRESS

shape of the reference model particles (see Fig. 3). Thus, despite substantial morphological simplifications in all three classes of model particles, we find a correspondence in overall shape between the morphologically complex reference particles and the highly symmetric model particles.

Figure 12 compares the mean coated convex polyhedra model results as a reference (blue) with the best fits of the inhomogeneous (green), homogeneous (orange) superellipsoids, and the cube-sphere hybrid (red). The extinction-to-backscatter ratio was not included in the calculation of the best fit, as this would implicitly weigh C_{ext} and C_{bak} stronger than δ_l. The best fit of the inhomogeneous superellipsoids result in the smallest deviations from the coated convex polyhedra model for C_{ext} at $r_0 = 0.33\,\mu$m and $r_0 = 0.67\,\mu$m, as well as for δ_l at $r_0 = 0.33\,\mu$m and $r_0 = 1.0\,\mu$m. For C_{bak}, C_{ext}, and S_p at $r_0 = 1.0\,\mu$m, and S_p at $r_0 = 0.67\,\mu$m the best fit of the cube-sphere hybrid model results in the smallest deviations from the reference model. For the remaining quantities the homogeneous superellipsoidal model results in the smallest deviations. Thus, none of the three models sticks out as significantly superior to the other two. The discrepancies in backscattering and extinction cross section, despite the overall consistent trends, between the reference and the best fits of the morphologically simpler models, result in rather poor agreement between the models with respect to the extinction-to-backscatter ratio. The differences are especially apparent for $r_0 = 0.67\,\mu$m; here S_p obtained with the reference model

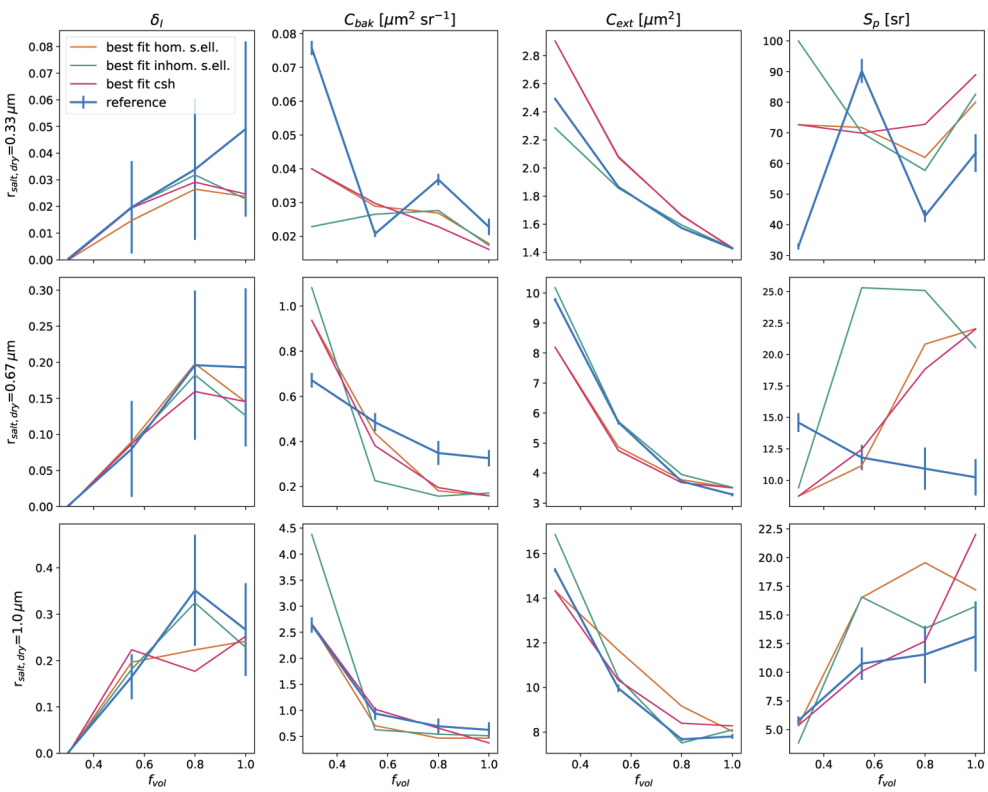

Fig. 12. Comparison of δ_l, C_{bak}, C_{ext}, and S_p (columns from left to right) for $r_0 = 0.33\,\mu$m, (top row) $r_0 = 0.67\,\mu$m (middle row), and $r_0 = 1.0\,\mu$m (bottom row). Blue lines show the arithmetic mean of the reference model. The error bars denote the standard deviation. Orange, green, and red indicate the best fit for homogeneous (denoted as hom. s. ell. in the legend), inhomogeneous superellipsoids (referred to as inhom. s. ell.), and cube-sphere hybrids (denoted as csh) respectively.

Optics EXPRESS

decreases with increasing f_{vol}, whereas, S_p for the best fit of the simplified models increase. For applications with less emphasis on the depolarization ratios these differences could be reduced by increasing the weight on the optical cross sections, or by including the lidar ratio in the error metric in Eq. (9).

Examples for the geometries giving the best fit for $r_0 = 0.67\ \mu$m and $f_{\mathrm{vol}} = 0.55$ are shown in Fig. 13. Furthest left is the geometry of coated polyhedra (with $N_c = 50$), which gives δ_l and C_{bak} values closest to the mean value. Thus, this specific geometric realization is optically most representative for the ensemble consisting of 15 different realizations (three values of N_c with five different stochastic realizations each). The remaining three geometries are, from left to right - a homogeneous superellipsoid (with $n = 0.4$), an inhomogeneous superellipsoid (with $n = 0.7$), and a cube-sphere hybrid (with $\eta = 0.4$).

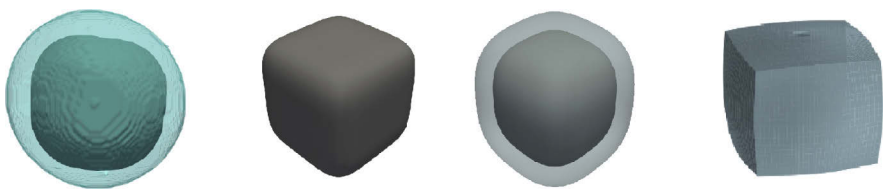

Fig. 13. Coated polyhedron with $r_0 = 0.67\ \mu$m, $f_{\mathrm{vol}} = 0.55$, and $N_c = 50$ (left), which gives values of δ_l and C_{bak} closest to the mean, shown in Fig. 12. The other model particles show the respective realization giving the best fit. From left to right these are - a homogeneous superellipsoid ($n = 0.4$), an inhomogeneous superellipsoid ($n = 0.7$), and a cube-sphere hybrid ($\eta = 0.4$).

The non-zero depolarization ratio of the reference geometry shown here stems entirely from the nonspherical salt-core, as the watery coating is already spherical. The simplified geometries indicate, that the overall non-sphericity of the superellipsoids and the cube-sphere hybrids are not directly mirrored by the respective coated polyhedra. However, the inhomogeneous superellipsoid is closer to a spherical form, than the other two geometries. The best-fit roundness parameters of the inhomogeneous superellipsoidals, as can be seen in Figs. 9–11, are always equal to or larger than those of the homogeneous superellipsoids, i.e. $n_{\mathrm{inhomogeneous}} \geq n_{\mathrm{homogeneous}}$. Thus, effects from centered inhomogeneities in the inhomogeneous superellipsoids can be compensated by less spherical homogeneous superellipsoids. This is a remarkable result, as inhomogeneity can, in other cases, have such a profound effect on optical properties that attempts to mimic their effect by use of homogeneous model particles have failed. For instance, for particles with a refractive index of $m = 1.5 + 0.002\mathrm{i}$ (representative of silicate particles) homogeneous spheroids are capable of reproducing optical properties of other homogeneous particles of various shapes, including Gaussian random spheres and cubes. However, attempts to mimic the optical properties of inhomogeneous spheroids with multiple spherical air inclusions by use of homogeneous spheroids were unsuccessful, even when trying different effective medium approaches, different metrics for the equivalent size of homogeneous and inhomogeneous particles, and when fitting a shape-distribution of the homogeneous model particles to the inhomogeneous reference particles [63]. In our case, inhomogeneity still has a significant effect, which is consistent with what has been previously seen for mineral dust [63,64]. However, the effect is not so profound that the optical properties cannot be mimicked by use of adequately selected homogeneous model particles. A plausible explanation is that in our study the optical contrast between the brine coating and the salt core is relatively small, which moderates the impact of inhomogeneity on optical properties.

Optics EXPRESS

5. Discussion and conclusion

The first question we formulated in the introduction concerned the performance of a detailed reference model that describes the water-uptake process by use of physically plausible assumptions. Qualitatively, the model largely behaves as expected. The depolarization ratio converges to zero as more water is added, resulting in a spherical geometry. At the same time the optical cross sections increase due to particle growth.

More quantitatively, we found that the proposed coated polyhedra model covers mean values of δ_l ranging from 0 to 0.35. The optical cross sections in this study, which are more directly linked with the particle size than δ_l, cover ranges in case of C_{bak} from 0.025 to 2.6 $\mu\text{m}^2\,\text{sr}^{-1}$, and in case of C_{ext} from 1.4 to 15.5 μm^2. The lidar ratio S_p ranges between 5 and 90 sr. It must be emphasized that these are results for individual particles, which cannot be directly compared to reported lidar field observations, as presented in Tab. 1, since these refer to particle ensembles averaged over a size distribution. Nevertheless, we can attempt to make a first assessment whether or not size-averaged optical properties are likely to fall within the range of reported measurements.

Table 1. Reported values of δ_l and S_p at $\lambda = 0.532\,\mu$m from lidar field measurements of marine aerosol, including the reported values of RH. The values of S_p from [65] (*) were assumed to be $S_p = 20$ sr, based on values from [66]. In [67] values of δ_l<5% were reported for a wide range of RH (**), without giving the explicit range. * marks mean values of S_p reported for the entire case study.**

location	δ_l (%)	S_p (sr)	RH (%)	reference
Praia, Cape Verde	3	18	-	[68]
Praia, Cape Verde	2 ± 2	19 ± 2	-	[66]
Praia, Cape Verde	3 ± 1	18 ± 5	-	[69]
Atlantic Ocean (west of Western Sahara)	<2	(20)*	~ 75 – 90	[65]
Atlantic Ocean (west of Western Sahara)	8	(20)*	10	[65]
Carribean Sea	<10	15 – 25	-	[70]
Fukuoka, Japan	6 ± 3	29.7 ± 2	64	[71]
Husbands, Barbados	≤ 2	23.2	80	[25]
Husbands, Barbados	14.8 ± 3.5	25.3	40	[25]
Tokyo, Japan	1-3	-	~ 70	[27]
Tokyo, Japan	10	-	<50	[27]
Tokyo, Japan	2-5	-	60 – 70	[27]
Tokyo, Japan	5-8	-	~ 60	[27]
Tokyo, Japan	1-2	-	80 – 90	[27]
Atlantic Ocean (near Cape Town)	9	13 ± 3	<40	[72]
Atlantic Ocean (near Cape Town)	<1	23 ± 1	>80	[72]
Nagoya, Japan	<5	-	**	[67]
Nagoya, Japan	10 – 20	-	25-45	[67]
Southern Ocean (54.4°S, 145.9°E)	25-29	10 ± 2***	11-18	[73]
Southern Ocean (54.4°S, 145.9°E)	<1.5	10 ± 2***	>60	[73]
Southern Ocean (45.2°S, 145.9°E)	>25	16 ± 2***	<20	[73]
Southern Ocean (45.2°S, 145.9°E)	<1	16 ± 2***	>60	[73]

There are several reports of lidar field measurements, as well as two studies that investigated satellite-borne lidar measurements of marine aerosol over a larger spatial and temporal scale [74,75]. In [74] a global mean value of S_p for marine aerosol was reported as $S_p = 26$ sr. This study was based on night-time observations by the Cloud-Aerosol Lidar with Orthogonal Polarization (CALIOP) satellite sensor between December 2007 and November 2010. S_p was

Optics EXPRESS

found to depend on the surface wind speed u and ranges between $S_p = 22 \pm 7$ sr (u>15 m s^{-1}) and 32 ± 7 sr (u<4 m s−1). Another study [75] used night-time data measured by the CALIOP instrument during the austral winter in a ten year (2007-2016) time period over the Southern Ocean (40°S-65°S). In [75] δ_l for clean marine aerosol, as identified in the CALIOP product, was found to range between 6% (RH= 100%) and 17% (RH= 0%).

Summarizing the reported observations in Table 1, the linear depolarization ratio of marine aerosol covers a range between <1% and 25 − 29%, although most values are below 20%. The reported measured extinction-to-backscatter ratio varies between 10 ± 2 sr and 32 ± 17, but $S_p = 10 \pm 2$ sr [73] and $S_p = 13 \pm 3$ sr [72] appear to be low outliers.

In many cases, our reference model falls within the range of reported measurements, but at some individual sizes the model exceeds the measurements. For example, the values of S_p at $r_0 = 0.33\,\mu$m and δ_l at $r_0 = 1.0\,\mu$m, exceeds the range of reported observations. However, in [19] we reported for small, individual superellipsoids ($r_0 = 0.25\,\mu$m, $m = 1.5484 + i0$) values of $S_p \sim 100$ sr, which are clearly larger than the observation-derived lidar ratios. But after size-averaging we obtained a range of $S_p = 12 - 20$ sr. This indicates that size-averaging is likely to quench the extreme values observed for some isolated particle sizes, and to yield ensemble-averaged values of S_p and δ_l more in line with the observations.

Further, the coated polyhedra model can be fine-tuned by changing the number of randomly placed points N_c, thus affecting the salt core's initial shape or by tuning the surface potential calculations, affecting the shape of the coating and of the partially dissolved salt core. Future guidance would need to be provided by laboratory studies.

We can conclude that this prospecting study shows sufficient promise to warrant further investigation of size-averaged optical properties computed with our reference model. Owing to the high computational requirements, this will be a computationally very demanding follow-up study.

The second question we formulated in the introduction was whether or not the particle can still depolarize once the core and the shell have reached spherical shape, owing to a variation of the positioning of the salt core within the brine mantel. The results of the non-concentric spherical shell model suggest that considerable values of the linear depolarization ratio (up to ∼ 0.5) can be induced by off-center inhomogeneities, especially for particles with f_{vol}<0.45. This is of comparable magnitude as the effect that a nonspherical coating can have on depolarization. This is a very unexpected result. We know from studies of coated soot aerosols that the positioning of the soot core within the mantle has a rather modest effect on the depolarization ratio (e.g. [76]). While coated soot particles are characterized by a high optical contrast between the soot core and the coating, our brine-coated salt particles are composed of optically very similar materials. It is entirely unexpected that inhomogeneity in a composite particle of such low optical contrast can have such a profound impact on depolarization. However, we emphasize that we obtained the largest values of δ_l for individual sizes and volume fractions. Size-averaging is likely to significantly moderate the effect of core positioning on depolarization. We note also that we currently know very little about the positioning of the salt core within the brine mantle. Our investigation was motivated by energy potential calculations presented in [39], which suggest that it is more likely for the core to be positioned off-center close to the surface of the coating. But further measurements are required to determine if and how frequently such off-center inhomogeneities can be observed in partially dissolved sea-salt crystals.

The third question concerned the capacity of simplified model particles to reproduce the optical properties of the reference model. We found that both superellipsoidal models and the cube-sphere hybrid model cover a large range of optical properties. By changing the respective model particle's non-sphericity, quantified either by n in case of superellipsoids or by η in case of cube-sphere hybrids, the optical properties can be fitted to different stages of the partial dissolution process of sea salt particles, as described by the coated polyhedra model. All three models can

Optics EXPRESS

reproduce the optical properties comparatively well, with the homogeneous superellipsoidal model resulting in the smallest deviations from the convex polyhedra model in five of twelve cases, as defined by optical properties and r_0. The lidar ratio S_p was most challenging to reproduce. However, a likely explanation is that S_p was not explicitly accounted for in the error metric in Eq. (9) that was employed in determining the best-fit model particles.

Th final question was if we can gain some insight into the relevance of different morphological features for the optical properties. We found that, despite the low optical contrast between the salt core and the brine mantle, inhomogeneity can have a strong impact on depolarization. However, we also found that both homogeneous superellipsoids and cube-sphere hybrids can compensate for inhomogeneities. In fact, the overall nonsphericity of the coating seems to be a key morphological parameter that impacts the depolarization ratio, but also the backscattering cross section. Further, a comparison between the homogeneous superellipsoidal model and the cube-sphere hybrids revealed that both models give very similar results. The main morphological difference between the two models is that the former accounts for rounding of the particle edges, while the latter does not. This indicates that the overall shape has a significantly more prominent impact on the optical properties than rounding of edges and corners.

One important question that we did not address is the sensitivity to the refractive index of sea salt. For dry marine aerosols we used the refractive index of sodium chloride. Under realistic conditions, organic and inorganic impurities can modulate the refractive index of sea-salt particles. A recent study based on superellipsoids [19] showed that a decrease in the real part and an increase in the imaginary part, which would be typical for organic impurities, can lower the backscattering cross section and raise the lidar ratio. The depolarization ratio will mainly increase with decreasing real part, and decrease with increasing imaginary part of the refractive index.

Further refinements of the coated polyhedra and superellipsoid models are conceivable, e.g., by considering non-unity aspect ratios of the superellipsoids, i.e. $a = b \neq c$ or $a \neq b \neq c$. The search for suitable simplified models could be widened accordingly. However, development of such highly tunable models with several free parameters will have to rely on guidance provided by laboratory measurements, which are currently in short supply.

Funding. Vetenskapsrådet (2016-03499); Swedish National Space Agency (126/19).

Acknowledgments. We are grateful to Dan Mackowski for making his MSTM code publicly available and to Maxim Yurkin and Alfons Hoekstra for making their ADDA code publicly available. The calculations were partly performed by resources provided by the Swedish National Infrastructure for Computing (SNIC) at Chalmers Centre for Computational Science and Engineering (C3SE).

Disclosures. The authors declare no conflicts of interest.

Data availability. Model output data presented in Figs. 5 – 12 and input geometries of coated convex polyhedra are publicly available in [77].

References

1. O. Boucher, *Atmospheric Aerosols - Properties and Climate Impacts* (Springer, 2015).
2. P. R. Buseck and M. Pósfai, "Airborne minerals and related aerosol particles: Effects on climate and the environment," Proc. Natl. Acad. Sci. U. S. A. **96**(7), 3372–3379 (1999).
3. S. M. King, A. C. Butcher, T. Rosenoern, E. Coz, K. I. Lieke, G. de Leeuw, E. D. Nilsson, and M. Bilde, "Investigating primary marine aerosol properties: CCN activity of sea salt and mixed inorganic-organic particles," Environ. Sci. Technol. **46**(19), 10405–10412 (2012).
4. D. M. Murphy, J. R. Anderson, P. K. Quinn, L. M. McInnes, F. J. Brechtel, S. M. Kreidenweis, A. M. Middlebrook, M. Pósfai, D. S. Thomson, and P. R. Buseck, "Influence of sea-salt on aerosol radiative properties in the Southern Ocean marine boundary layer," Nature **392**(6671), 62–65 (1998).
5. G. Meira, C. Andrade, C. Alonso, I. Padaratz, and J. Borba, "Modelling sea-salt transport and deposition in marine atmosphere zone – a tool for corrosion studies," Corros. Sci. **50**(9), 2724–2731 (2008).
6. N. C. Wells, *The Atmosphere and Ocean: A Physical Introduction* (John Wiley & Sons, Inc., 2011), 3rd ed.
7. J. W. Chi, W. J. Li, D. Z. Zhang, J. C. Zhang, Y. T. Lin, X. J. Shen, J. Y. Sun, J. M. Chen, X. Y. Zhang, Y. M. Zhang, and W. X. Wang, "Sea salt aerosols as a reactive surface for inorganic and organic acidic gases in the Arctic troposphere," Atmos. Chem. Phys. **15**(19), 11341–11353 (2015).

Optics EXPRESS

8. R. Irshad, R. G. Grainger, D. M. Peters, R. A. McPheat, K. M. Smith, and G. Thomas, "Laboratory measurements of the optical properties of sea salt aerosol," Atmos. Chem. Phys. **9**(1), 221–230 (2009).
9. M. Pósfai, J. R. Anderson, P. R. Buseck, and H. Sievering, "Compositional variations of sea-salt-mode aerosol particles from the North Atlantic," J. Geophys. Res. **100**(D11), 23063–23074 (1995).
10. I. N. Tang, A. C. Tridico, and K. H. Fung, "Thermodynamic and optical properties of sea salt aerosols," J. Geophys. Res. **102**(D19), 23269–23275 (1997).
11. S. Ueda, Y. Hirose, K. Miura, and H. Okochi, "Individual aerosol particles in and below clouds along a Mt. Fuji slope: Modification of sea-salt-containing particles by in-cloud processing," Atmos. Res. **137**, 216–227 (2014).
12. J. P. Patterson, D. B. Collins, J. M. Michaud, J. L. Axson, C. M. Sultana, T. Moser, A. C. Dommer, J. Conner, V. H. Grassian, M. D. Stokes, G. B. Deane, J. E. Evans, M. D. Burkart, K. A. Prather, and N. C. Gianneschi, "Sea spray aerosol structure and composition using cryogenic transmission electron microscopy," ACS Cent. Sci. **2**(1), 40–47 (2016).
13. E. P. Shettle and R. W. Fenn, "Models for the aerosols of the lower atmosphere and the effects of humidity variations on their optical properties," AFGL Technical Report AFGL-TR-79–021A, Air Force Geophysics Laboratory (1979).
14. J. Zeng, G. Zhang, S. Long, K. Liu, L. Cao, L. Bao, and Y. Li, "Sea salt deliquescence and crystallization in atmosphere: an in situ investigation using x-ray phase contrast imaging," Surf. Interface Anal. **45**(5), 930–936 (2013).
15. J. H. Seinfeld and S. N. Pandis, *Atmospheric Chemistry and Physics : From Air Pollution to Climate Change* (John Wiley & Sons, Incorporated, 2016).
16. P. Zieger, O. Väisänen, J. C. Corbin, D. G. Partridge, S. Bastelberger, M. Mousavi-Fard, B. Rosati, M. Gysel, U. K. Krieger, C. Leck, A. Nenes, I. Riipinen, A. Virtanen, and M. E. Salter, "Revising the hygroscopicity of inorganic sea salt particles," Nat. Commun. **8**(1), 15883 (2017).
17. O. Laskina, H. S. Morris, J. R. Grandquist, Z. Qin, E. A. Stone, A. V. Tivanski, and V. H. Grassian, "Size matters in the water uptake and hygroscopic growth of atmospherically relevant multicomponent aerosol particles," J. Phys. Chem. A **119**(19), 4489–4497 (2015). PMID: 25521409.
18. T. Sakai, T. Nagai, Y. Zaizen, and Y. Mano, "Backscattering linear depolarization ratio measurements of mineral, sea-salt, and ammonium sulfate particles simulated in a laboratory chamber," Appl. Opt. **49**(23), 4441–4449 (2010).
19. F. Kanngießer and M. Kahnert, "Modeling optical properties of non-cubical sea salt particles," J. Geophys. Res.: Atmos. **126**(4), e2020JD033674 (2021). E2020JD033674 2020JD033674.
20. M. Kahnert and E. Andersson, "How much information do extinction and backscattering measurements contain about the chemical composition of atmospheric aerosol?" Atmos. Chem. Phys. **17**(5), 3423–3444 (2017).
21. R. Kahn, P. Banerjee, D. McDonald, and D. J. Diner, "Sensitivity of multiangle imaging to aerosol optical depth and to pure-particle size distribution and composition over ocean," J. Geophys. Res. **103**(D24), 32195–32213 (1998).
22. F. Barnaba and G. P. Gobbi, "Lidar estimation of tropospheric aerosol extinction, surface area and volume: Maritime and desert-dust cases," J. Geophys. Res. **106**(D3), 3005–3018 (2001).
23. K. Chamaillard, C. Kleefeld, S. Jennings, D. Ceburnis, and C. O'Dowd, "Light scattering properties of sea-salt aerosol particles inferred from modeling studies and ground-based measurements," J. Quant. Spectrosc. Radiat. Transfer **101**(3), 498–511 (2006). Light in Planetary Atmospheres and Other Particulate Media.
24. K. Adachi and P. R. Buseck, "Changes in shape and composition of sea-salt particles upon aging in an urban atmosphere," Atmos. Environ. **100**, 1–9 (2015).
25. M. Haarig, A. Ansmann, J. Gasteiger, K. Kandler, D. Althausen, H. Baars, M. Radenz, and D. A. Farrell, "Dry versus wet marine particle optical properties: RH dependence of depolarization ratio, backscatter, and extinction from multiwavelength lidar measurements during SALTRACE," Atmos. Chem. Phys. **17**(23), 14199–14217 (2017).
26. G. David, B. Thomas, T. Nousiainen, A. Miffre, and P. Rairoux, "Retrieving simulated volcanic, desert dust and sea-salt particle properties from two/three-component particle mixtures using UV-VIS polarization lidar and T matrix," Atmos. Chem. Phys. **13**(14), 6757–6776 (2013).
27. T. H. Murayama, H. Okamoto, N. Kaneyasu, H. Kamataki, and K. Miura, "Application of lidar depolarization measurement in the atmospheric boundary layer: Effects of dust and sea-salt particles," J. Geophys. Res. **104**(D24), 31781–31792 (1999).
28. L. Bi, W. Lin, Z. Wang, X. Tang, X. Zhang, and B. Yi, "Optical modeling of sea salt aerosols:the effects of nonsphericity and inhomogeneity," J. Geophys. Res. **123**(1), 543–558 (2018).
29. Z. Wang, L. Bi, B. Yi, and X. Zhang, "How the inhomogeneity of wet sea salt aerosols affects direct radiative forcing," Geophys. Res. Lett. **46**(3), 1805–1813 (2019).
30. M. Li, L. Bi, W. Lin, F. Weng, S. He, and X. Zhang, "The inhomogeneity effect of sea salt aerosols on the TOA polarized radiance at the scattering angles ranging from 170° to 175°," IEEE Trans. Geosci. Remote Sens. pp. 1–12 (2021).
31. L. Liu and M. I. Mishchenko, "Scattering and radiative properties of morphologically complex carbonaceous aerosols: a systematic modeling study," Remote Sens. **10**(10), 1634 (2018).
32. F. Kanngiesser and M. Kahnert, "Coating material-dependent differences in modelled lidar-measurable quantities for heavily coated soot particles," Opt. Express **27**(25), 36368–36387 (2019).
33. P. Gwaze, G. Helas, H. J. Annegarn, J. Huth, and S. J. Piketh, "Physical, chemical and optical properties of aerosol particles collected over Cape Town during winter haze episodes," S. Afr. J. Sci. **103**, 35–43 (2007).

Optics EXPRESS

34. L. M. McInnes, D. S. Covert, P. K. Quinn, and M. S. Germani, "Measurements of chloride depletion and sulfur enrichment in individual sea-salt particles collected from the remote marine boundary layer," J. Geophys. Res.: Atmos. **99**(D4), 8257–8268 (1994).
35. A. Peart and J. R. G. Evans, "Study of sea salt particles launched by bubble burst," Bub. Sci. Eng. Technol. **3**(2), 64–72 (2011).
36. M. E. Wise, G. Biskos, S. T. Martin, L. M. Russell, and P. R. Buseck, "Phase transitions of single salt particles studied using a transmission electron microscope with an environmental cell," Aerosol Sci. Technol. **39**(9), 849–856 (2005).
37. A. Torge, A. Macke, B. Heinold, and J. Wauer, "Solar radiative transfer simulations in Saharan dust plumes: particle shapes and 3-D effect," Tellus B **63**(4), 770–780 (2011).
38. H. Ishimoto, R. Kudo, and K. Adachi, "A shape model of internally mixed soot particles derived from artificial surface tension," Atmos. Meas. Tech. **12**(1), 107–118 (2019).
39. T. Corti, "Messung und Modellierung intern gemischter Seesalzaerosole," mathesis, Institut für Atmosphäre und Klima der ETH Zürich, Departement Umweltnaturwissenschaften (2002).
40. K. A. Fuller, "Scattering and absorption cross sections of compounded spheres. iii. spheres containing arbitrarily located spherical inhomogeneities," J. Opt. Soc. Am. A **12**(5), 893–904 (1995).
41. L. Bi, W. Lin, D. Liu, and K. Zhang, "Assessing the depolarization capabilities of nonspherical particles in a super-ellipsoidal shape space," Opt. Express **26**(2), 1726–1742 (2018).
42. W. Lin, L. Bi, and O. Dubovik, "Assessing superspheroids in modeling the scattering matrices of dust aerosols," J. Geophys. Res.: Atmos. **123**(24), 13917–13943 (2018).
43. A. H. Barr, "Superquadrics and angle-preserving transformations," IEEE Comput. Grap. Appl. **1**(1), 11–23 (1981).
44. T. Wriedt, "Using the T-matrix method for light scattering computations by non-axisymmetric particles: superellipsoids and realistically shaped particles," Part. Part. Syst. Charact. **19**(4), 256–268 (2002).
45. J. C. Maxwell Garnett, "XII. colours in metal glasses and in metallic films," Phil. Trans. R. Soc. Lond. A **203**(359-371), 385–420 (1904).
46. P. C. Waterman, "Symmetry, unitarity, and geometry in electromagnetic scattering," Phys. Rev. D **3**(4), 825–839 (1971).
47. M. I. Mishchenko and J. W. Hovenier, "Depolarization of light backscattered by randomly oriented nonspherical particles," Opt. Lett. **20**(12), 1356–1358 (1995).
48. J. Gasteiger, M. Wiegner, S. Groß, V. Freudenthaler, C. Toledano, M. Tesche, and K. Kandler, "Modelling lidar-relevant optical properties of complex mineral dust aerosols," Tellus B **63**(4), 725–741 (2011).
49. E. E. Eloranta, *High Spectral Resolution Lidar* (Springer New York, 2005), pp. 143–163.
50. U. Wandinger, *Raman Lidar* (Springer New York, , 2005), pp. 241–271.
51. J. Eldridge and E. D. Palik, "- sodium chloride (NaCl)," in *Handbook of Optical Constants of Solids*, E. D. Palik, ed. (Academic Press, 1997), pp. 775–793.
52. X. Li, L. Liu, J. Zhao, and J. Tan, "Optical properties of sodium chloride solution within the spectral range from 300 to 2500 nm at room temperature," Appl. Spectrosc. **69**(5), 635–640 (2015).
53. M. A. Yurkin and A. G. Hoekstra, "The discrete dipole approximation: an overview and recent developments," J. Quant. Spectrosc. Radiat. Transfer **106**(1-3), 558–589 (2007). IX Conference on Electromagnetic and Light Scattering by Non-Spherical Particles.
54. M. A. Yurkin and A. G. Hoekstra, "The discrete-dipole-approximation code ADDA: capabilities and known limitations," J. Quant. Spectrosc. Radiat. Transfer **112**(13), 2234–2247 (2011).
55. D. Mackowski and M. Mishchenko, "A multiple sphere T-matrix Fortran code for use on parallel computer clusters," J. Quant. Spectrosc. Radiat. Transfer **112**(13), 2182–2192 (2011). Polarimetric Detection, Characterization, and Remote Sensing.
56. F. M. Schulz, K. Stamnes, and J. J. Stamnes, "Point group symmetries in electromagnetic scattering," J. Opt. Soc. Am. A **16**(4), 853–865 (1999).
57. F. M. Kahnert, J. J. Stamnes, and K. Stamnes, "Application of the extended boundary condition method to homogeneous particles with point group symmetries," Appl. Opt. **40**(18), 3110–3123 (2001).
58. M. Kahnert, "Irreducible representations of finite groups in the T matrix formulation of the electromagnetic scattering problem," J. Opt. Soc. Am. A **22**(6), 1187–1199 (2005).
59. N. G. Khlebtsov, "Orientational averaging of light-scattering observables in the T-matrix approach," Appl. Opt. **31**(25), 5359–5365 (1992).
60. D. W. Mackowski and M. I. Mishchenko, "Calculation of the T matrix and the scattering matrix for ensembles of spheres," J. Opt. Soc. Am. A **13**(11), 2266–2278 (1996).
61. M. Kahnert, "The T-matrix code Tsym for homogeneous dielectric particles with finite symmetries," J. Quant. Spectrosc. Radiat. Transfer **123**, 62–78 (2013).
62. M. Kahnert, "michaelkahnert/tsym-5.2: Tsym 5.2," (2020).
63. T. Nousiainen, M. Kahnert, and H. Lindqvist, "Can particle shape information be retrieved from light-scattering observations using spheroidal model particles?" J. Quant. Spectrosc. Radiat. Transfer **112**(13), 2213–2225 (2011).
64. M. Kahnert, "Modelling radiometric properties of inhomogeneous mineral dust particles: Applicability and limitations of effective medium theories," J. Quant. Spectrosc. Radiat. Transfer **152**, 16–27 (2015).
65. Z. Yin, A. Ansmann, H. Baars, P. Seifert, R. Engelmann, M. Radenz, C. Jimenez, A. Herzog, K. Ohneiser, K. Hanbuch, L. Blarel, P. Goloub, G. Dubois, S. Victori, and F. Maupin, "Aerosol measurements with a shipborne

Optics EXPRESS

sun–sky–lunar photometer and collocated multiwavelength Raman polarization lidar over the Atlantic Ocean," Atmos. Meas. Tech. **12**(10), 5685–5698 (2019).
66. S. Groß, M. Tesche, V. Freudenthaler, C. Toledano, M. Wiegner, A. Ansmann, D. Althausen, and M. Seefeldner, "Characterization of Saharan dust, marine aerosols and mixtures of biomass-burning aerosols and dust by means of multi-wavelength depolarization and Raman lidar measurements during SAMUM 2," Tellus B **63**(4), 706–724 (2011).
67. T. Sakai, T. Shibata, S.-A. Kwon, Y.-S. Kim, K. Tamura, and Y. Iwasaka, "Free tropospheric aerosol backscatter, depolarization ratio, and relative humidity measured with the Raman lidar at Nagoya in 1994–1997: contributions of aerosols from the Asian Continent and the Pacific Ocean," Atmos. Environ. **34**(3), 431–442 (2000).
68. M. Tesche, S. Gross, A. Ansmann, D. Müller, D. Althausen, V. Freudenthaler, and M. Esselborn, "Profiling of Saharan dust and biomass-burning smoke with multiwavelength polarization Raman lidar at Cape Verde," Tellus B **63**(4), 649–676 (2011).
69. S. Groß, M. Esselborn, B. Weinzierl, M. Wirth, A. Fix, and A. Petzold, "Aerosol classification by airborne high spectral resolution lidar observations," Atmos. Chem. Phys. **13**(5), 2487–2505 (2013).
70. S. P. Burton, R. A. Ferrare, C. A. Hostetler, J. W. Hair, R. R. Rogers, M. D. Obland, C. F. Butler, A. L. Cook, D. B. Harper, and K. D. Froyd, "Aerosol classification using airborne high spectral resolution lidar measurements – methodology and examples," Atmos. Meas. Tech. **5**(1), 73–98 (2012).
71. Y. Hara, T. Nishizawa, N. Sugimoto, I. Matsui, X. Pan, H. Kobayashi, K. Osada, and I. Uno, "Optical properties of mixed aerosol layers over Japan derived with multi-wavelength Mie–Raman lidar system," J. Quant. Spectrosc. Radiat. Transfer **188**, 20–27 (2017).
72. S. Bohlmann, H. Baars, M. Radenz, R. Engelmann, and A. Macke, "Ship-borne aerosol profiling with lidar over the Atlantic Ocean: from pure marine conditions to complex dust–smoke mixtures," Atmos. Chem. Phys. **18**(13), 9661–9679 (2018).
73. S. P. Alexander and A. Protat, "Vertical profiling of aerosols with a combined Raman-elastic backscatter lidar in the remote Southern Ocean marine boundary layer (43–66°S, 132–150°E)," J. Geophys. Res.: Atmos. **124**(22), 12107–12125 (2019).
74. K. W. Dawson, N. Meskhidze, D. Josset, and S. Gassó, "Spaceborne observations of the lidar ratio of marine aerosols," Atmos. Chem. Phys. **15**(6), 3241–3255 (2015).
75. M. A. Thomas, A. Devasthale, and M. Kahnert, "Marine aerosol properties over the Southern Ocean in relation to the wintertime meteorological conditions," Atmos. Chem. Phys. Discuss. **2021**, 1–22 (2021).
76. M. Kahnert and F. Kanngießer, "Aerosol optics model for black carbon applicable to remote sensing, chemical data assimilation, and climate modelling," Opt. Express **29**(7), 10639–10658 (2021).
77. F. Kanngießer and M. Kahnert, "Optical properties of water-coated sea salt aerosol," (2021).